Deposition of nanoporous BiVO4 thin-film photocatalyst by reactive magnetron sputtering: Effect of total pressure and substrate

Siavash Bakhtiarnia, Saeed Sheibani, Alain Billard, Eric Aubry, Mohammad Arab Pour Yazdi

Deposition of nanoporous $BiVO_4$ thin-film photocatalyst by reactive magnetron sputtering: an investigation on the total pressure and substrate effect

Siavash Bakhtiarnia [a,b], Saeed Sheibani [a,*], Alain Billard [b], Eric Aubry [b], Mohammad Arab Pour Yazdi [b]

a. School of Metallurgy and Materials Engineering, College of Engineering, University of Tehran, Tehran, Iran.

b. Institut FEMTO-ST, UMR 6174, CNRS, Univ. Bourgogne Franche-Comté, 15B, Avenue des Montboucons, 25030 Besançon, France

*Corresponding author at School of Metallurgy and Materials Engineering, University of Tehran, P.O. Box 11155-4563, Tehran, Iran. Tel.: +98 21 61114068; Fax: +98 21 88006076.

E-mail address: ssheibani@ut.ac.ir (S. Sheibani).

Abstract

Nanoporous $BiVO_4$ thin films were deposited using the reactive magnetron sputtering in Ar and O_2 atmosphere, on various substrates, employing pulsed direct-current (DC) power supplies applied to metallic Bi and V targets for rapid deposition. The procedure was followed by a post-annealing treatment in the air to crystallize the photoactive monoclinic scheelite structure. The effect of total pressure and substrate is investigated on the crystal structure, morphology, microstructure, optical and photocatalytic properties of the films. The crystallization of monoclinic scheelite structure deposited on fused silica substrate started at 250 ˚C and the films were stable up to 600˚C. The morphology of the films is rather dense, despite the high sputtering pressure (> 2 Pa), with embedded nanopores. Among the thin films deposited on fused silica, the one deposited at 4.5 Pa exhibits the highest porosity (52 %), with the lowest bandgap (2.44 eV) and it showed the highest photocatalytic activity in the

degradation of Rhodamine-B (26 % after 7 h) under visible light irradiation. The film deposited on the silicon substrate exhibited the highest photoactivity (53 % after 7 h). Lack of hypsochromic shift in UV-Vis temporal absorption spectra shows the dominance of chromophore cleavage pathway in the photodecomposition.

Keywords: Photocatalyst; $BiVO_4$; Thin film; Sputtering; Nanoporous.

1. Introduction

Photocatalysis is considered to be one of the most interesting methods of wastewater treatment by producing strong oxidizing agents such as hydroxyl radicals ($^{\bullet}OH$), superoxide radicals ($^{\bullet}O_2^-$), and photogenerated holes in the presence of water and oxygen using solar energy [1]. A large number of semiconductors including TiO_2, ZnO, Cu_2O, CdS, FeS, Fe_2O_3, and perovskites have been studied as photocatalysts [2–4], among which, TiO_2 is the most popular due to its interesting properties like high photoactivity, good stability, and low cost [5–7]. However, its major drawback is being exclusively active in the UV region (only ~ 4 % of the solar spectrum) [8]. This has led to the development of photocatalysts with lower bandgap to be active under visible light. Bismuth vanadate ($BiVO_4$) with a relatively narrow bandgap ($E_g \approx 2.4$ eV for monoclinic scheelite structure), along with being low cost, chemically stable, and non-toxic has drawn lots of attention [9, 10]. $BiVO_4$ has three main crystal forms of monoclinic scheelite ($E_g \approx 2.4$ eV) [11], tetragonal scheelite ($E_g \approx 2.3$ eV), and tetragonal zircon-type structure ($E_g \approx 2.9$ eV) [12, 13]. The monoclinic scheelite structure shows higher photocatalytic activity thanks to the presence of O 2p and Bi 6s hybrid orbitals in the valence band resulting in a lower bandgap making it capable of absorbing visible light as opposed to TiO_2. It has also been reported that well-dispersed Bi 6s orbital contributes to the increase of photogenerated charge carriers [14, 15]. There are some studies available on the synthesis of $BiVO_4$ in nanopowder form through methods such as sol-gel [16], hydrothermal [17], solid-state reaction [18], and high energy ball-milling [19], which have a major drawback regarding recyclability and reusability. Thin films are one of the best solutions to this problem making photocatalysis more practical and economically viable.

There have been some researches on producing $BiVO_4$ thin films, though, few publications are focused on physical vapor deposition and sputtering in particular. Magnetron sputtering is a widely used thin-film production technique in the industry thanks to its high deposition rate,

uniformity, mass producibility, and clean production tool [20]. It also gives the ability to control the morphology by adjusting the deposition parameters [21, 22], which is a key aspect in enhancing $BiVO_4$ photoactivity [23] due to its poor photo charge carrier transfer and low specific surface [24]. In physical vapor deposition technology, the structural zone diagram (SZD), revisited by Anders [25], clearly shows that the morphology of deposited films is dependent on the deposition parameters like the normalized kinetic energy flux that affect film growth processes. It is shown that in the films deposited with high kinetic energy flux, the morphology is dense indicating as the zone T. On the other hand, zone 1 indicates a columnar porous morphology for the films deposited with low kinetic energy flux. The total pressure is considered as one of the main parameters affecting the normalized kinetic energy flux, thus affecting the film morphology. Nanoporous structures are one of the routes to overcome the low active surface problem of thin films. Previously, some researchers attempted to produce porous films involving low melting elements or alloys e.g. InSb [26], GaSb [27], Ge [28], Si_{1-x} Ge_x [29] through focused ion irradiation. The principle relies on the migration of ion-irradiation-induced point defects (Frenkel pairs; interstitial and vacancy), thus increasing the surface roughness and formation of porous structure [30]. To this day, no research has been focused on the nanoporous structure formation of thin films involving low-melting elements, Bi in particular, through the sputtering technique.

The present study aims to demonstrate the feasibility of producing nanoporous $BiVO_4$ thin films as the visible light active photocatalysts by a novel technique involving low melting metals and reactive DC magnetron sputtering using metallic Bi and V targets. Monocrystal silicon, fused silica, alumina, and glass, which have different structural, thermal, and optical properties were used as substrates. The effect of this synthesis conditions on the structure, morphology, porosity, optical and photocatalytic properties has not been studied so far.

Therefore, apart from previous studies, here, the total sputtering pressure and nature of the substrate as the parameters affecting the film properties were investigated.

2. Experimental procedure

2.1. Thin film deposition

$BiVO_4$ thin films were deposited by reactive DC magnetron sputtering using Bi and V metallic targets (Ø 50 mm × 3 mm, purity 99.9 at. %) in argon-oxygen gas mixtures. The sputtering reactor is a 90 L cylinder Alcatel 604 SCM (CIT Alcatel, Annecy, France) pumped down via a turbo-molecular-pump system that permits a residual vacuum below 10^{-4} Pa. The chamber was equipped with four circular planar and water-cooled magnetron sputtering sources and the rotating substrate holder was parallel to these sources at about 60 mm. The Bi and V targets were supplied with a pulsed DC advanced energy dual generator authorizing the control of the discharge power. The discharge power was adjusted for both targets to control the coating composition. Argon and oxygen flow rates were controlled with Brooks flowmeters and total sputtering pressure was measured using an MKS Baratron gauge. The details of the reactive magnetron sputtering reactor are described elsewhere [31]. Fused silica and glass slides (76 ×26 × 1 mm^3) were used as the main substrates to measure the composition and optical properties of the films. Alumina pellets and single crystal silicon wafers were also utilized as substrates to compare the effect of substrate on photocatalytic performance. Before each set, the substrates were cleaned with alcohol and soap and then rinsed with water. Then, they were placed on the substrate holder at 50 mm from the rotation substrate axis. All of the films were deposited at room temperature (without external heating) and at various total pressures. The total pressure was controlled by the Ar flow rate. The film thicknesses were controlled with the time of deposition, which could vary depending on the total pressure. The main sputtering parameters are summarized in Table 1.

Table 1. Fixed sputtering parameters during the deposition of $BiVO_4$ thin films.

Ar flow rate (sccm)	O_2 flow rate (sccm)	Total pressure (Pa)	Runtime (min)	Drawing distance (mm)
100, 200, 200	20	2.5, 4.5, 9.5	112, 240, 300	60
Targets	**Intensity (A)**	**Power (W)**	**Frequency (kHz)**	**T_{off} (μs)**
Bi	0.07, 0.07, 0.09	9, 9, 11	70	4
V	0.6, 0.64, 0.66	235, 247, 255	50	4

2.2. Characterization

The structural characterization of thin films was performed by Bragg-Brentano configuration XRD using a BRUKER D8 focus diffractometer (Bruker AXS, Karlsruhe, Germany) with a cobalt X-ray tube (Co $_{K\alpha1+\alpha2}$ radiations $\lambda_{\alpha1}$ = 0.178897 nm and $\lambda_{\alpha2}$ = 0.179278 nm) and equipped with a LynxEye linear detector. Film thickness was measured using a step method with an Altysurf profilometer (Altisurf 500), manufactured by Altimet. Before each measurement, the calibration of the experimental device was realized with a reference sample number 787569 accredited by the CETIM organization. The optical transmission and reflectance spectra of the films were measured using a Shimadzu UV-3600 UV-VIS-NIR spectrophotometer. The morphology was determined by a JEOL JSM 7800F FESEM. The chemical composition was analyzed by energy-dispersive X-ray spectroscopy (EDS, Bruker Nano, Berlin, Germany). The samples were carbon-coated before measurement to ensure sufficient electronic conductivity to avoid charges effect. The Bi and V atomic percentages are exclusively determined within the precision of the EDS measurements (the relative error is about 1 %) as EDS does not allow a precise estimation of the oxygen content in the films. **2.3. Photocatalytic performance**

The photocatalytic activity in the visible light range was evaluated by the photodegradation of RhB solution (5 mg/L) in a homemade setup. pH experiments were done to determine the

optimal condition of RhB photodegradation by $BiVO_4$ thin films and the results were published elsewhere [32]. It was found that the samples exhibit the highest photoactivity at pH = 3. Therefore the rest of the experiments were done at pH = 3. The amount of photocatalyst used in the experiments was 0.4 cm^2/mL, and each took place during 7 h of visible light illumination using a xenon light source (150 W, Lot-Oriel) emitting with a constant irradiance (150 cd mm^{-2}). A UV-cutoff filter ($\lambda > 400$ nm) was used to ensure that only the photons with the visible wavelengths reach the photocatalyst. The distance between the samples and the light source was fixed at 15 cm, and the photoreactor was placed in a water bath to keep the solution at room temperature (25 ˚C). The photocatalysts were immersed in the RhB solution 30 minutes before illumination to ensure the adsorption-desorption equilibrium. Every hour, 3 ml of the solution was retrieved to measure the absorbance at the maximum wavelength of RhB (554 nm) using a spectrophotometer (Libra S12-UV-Visible (200-999 nm) - BIOCHROM) to determine the concentration of the photodegraded sample using the Beer-Lambert law. The photocatalytic degradation reaction follows the kinetics of the Langmuir-Hinshelwood model and can be described by a pseudo-first-order model (Eq. (1)) when the dye concentration is low [33].

$$\ln \frac{C_0}{C} = k't \quad (1)$$

Where t is the time of irradiation in visible light, C_0 is the initial concentration, C is the concentration of the solution at time t and k′ is the rate constant. The constant k′ is therefore obtained by plotting ln (C_0/C) as a function of t, which is a straight line whose slope corresponds to k′.

3. Results and discussion

3.1. Composition, structure, and thermal stability

Fig. 1 shows the correlation between the metallic atomic ratio of Bi/V, measured by the EDS method, versus the discharge power ratio applied to each metallic target (P_{Bi}/P_V) for three

different total sputtering pressures of 2.5, 4.5, and 9.5 Pa. The desired metallic ratio to obtain the stoichiometric $BiVO_4$ is 1:1. Increasing the P_{Bi} results in a Bi-richer composition as expected, while increasing the total pressure develops V-rich composition, probably because of the Bi's higher atomic radius, consequently a lower mean free path and a lower quantity of Bi atoms incident to the growing film [34]. On the other hand, increasing the total pressure leads to a decrease in voltage that affects the spatial distribution of each target. In this case, we believe the spatial distribution of Bi is flatter than that of V resulting in a lower ratio of Bi/V sputtering flux in higher total pressures. According to the data shown in Fig. 1, this correlation follows an exponential trend owing to the same principle. The more the voltage is increased the less flat the spatial distribution becomes, increasing the atomic ratio of Bi/V. For the next parts, the power ratios are adjusted accordingly to achieve a Bi:V composition ratio of 1:1.

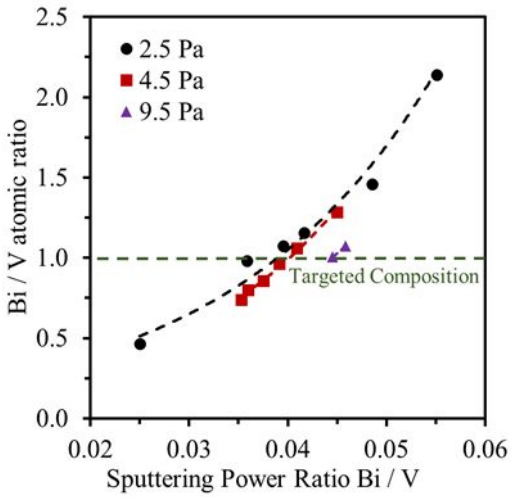

Fig. 1. The atomic composition ratio of Bi/V versus the sputtering power ratio applied to each metallic target (P_{Bi}/P_V) for different total sputtering pressures.

The as-deposited films were amorphous and a post-annealing treatment under air was necessary to crystallize the films no matter the deposition total pressure. Understanding the crystallization step of the films, determining the desired annealing temperature, and evaluating the thermal stability of the film, are of critical importance. Therefore, the thin films deposited on fused silica and glass substrates with a suitable composition (metallic ratio closed to 1:1)

were treated with a 2 h annealing process at different temperatures under the air atmosphere. Fig. 2 (a) provides the XRD patterns for the sample deposited on glass from 250 ˚C to 600 ˚C. The crystallization of the film deposited on glass starts at 300 ˚C and developed the desired monoclinic structure (m – $BiVO_4$, JCPDS No. 14-0688). However, some diffraction peaks were developed at temperatures over 350 ˚C, due to the contamination of the film by the diffusion of the sodium present in glass substrates. This new phase is identified as $NaBi_3V_2O_{10}$ (JCPDS No. 052-1226) [35] whose peaks become more intense as the temperature rises, as a result of the increase of sodium diffusion rates in the film, thus more contamination occurs. At 500 ˚C the peaks corresponding to monoclinic $BiVO_4$ are entirely removed in the XRD patterns. This result indicates that glass substrates are not suitable for the annealed $BiVO_4$ thin films because of sodium contamination. These observations are coherent with the previous report on the TiO_2 thin films sputtered on glass [36]. Fig. 2 (b) illustrates the XRD patterns of the films deposited on fused silica for the samples annealed at temperatures from 200 to 800 ˚C. As shown by the XRD patterns, the films deposited on fused silica started to crystallize at 50 ˚C lower than the films deposited on glass. This delay in crystallization observed for soda-lime glass was also reported for the sputtering of TiO_2 thin films due to the diffusion of the alkali elements that inhibits the nuclei formation [36]. The films were stable up to 550 ˚C, unlike what Venkatesan et al. [37] reported that the $Bi_2VO_{5.5}$ phase was observed after annealing at 410 ˚C in $BiVO_4$ thin film sputtered on a borosilicate glass substrate using the radiofrequency sputtering method. Here at 600 ˚C, the orthorhombic $Bi_2VO_{5.5}$ (o-$Bi_2VO_{5.5}$) structure with peaks at 2θ = 27.08˚ and 41˚ (JCPDS No. 42-0135) evolved along with orthorhombic vanadium pentoxide (o-V_2O_5), peak at 2θ = 25.26˚ (JCPDS No. 41-1426) as secondary phases, which suggests the segregation of vanadium. Fig. 2 (c) shows the evolution of the average crystallite size of the monoclinic $BiVO_4$, which was calculated by Scherrer's equation [38], against the temperature. As expected, the crystallite size rose linearly, as a consequence of raising the annealing

temperature. This investigation shows that 450 ˚C could be a suitable temperature to anneal the as-deposited thin films in avoiding secondary phase formation and film densification at higher temperatures.

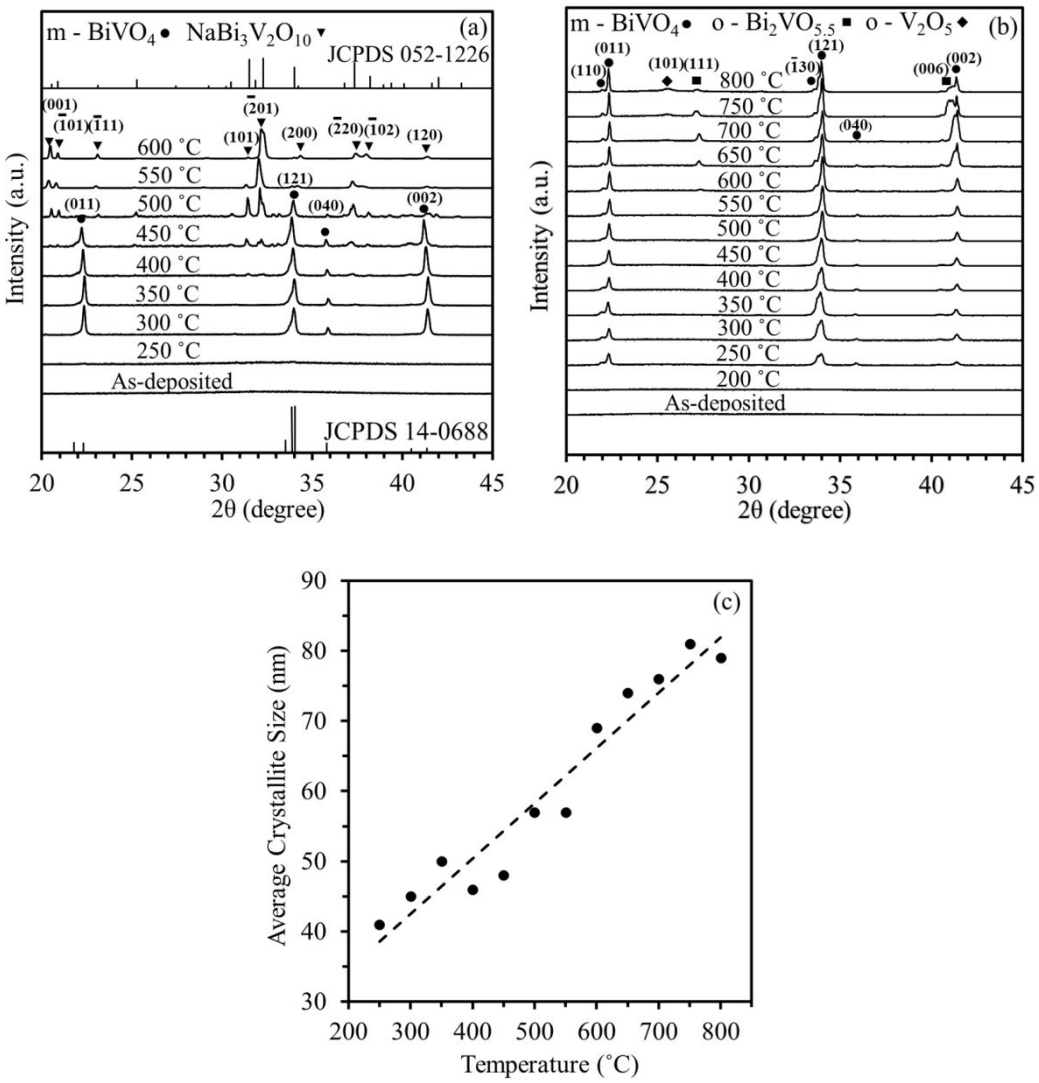

Fig. 2. (a) XRD patterns of the sample deposited on glass annealed at 250 to 600 ˚C. (b) XRD patterns of the $BiVO_4$ thin films deposited on fused silica substrate annealed at 200 to 800 ˚C. (c) The evolution of the average crystallite size versus annealing temperature.

Fig. 3 demonstrates the EDS spectra of the Bi, V, and O elemental mapping together with the corresponding SEM image of the $BiVO_4$ thin-film sample deposited on fused silica after 2 h of annealing at 450 ˚C in ambient atmosphere. On the latter, a network of cracks is

noticeable, which is not present on the as-deposited film (See Fig. 4 (a)). The formation of cracks is thus generated during the annealing and ascribed to the crystallization of the monoclinic scheelite phase, and to the difference of linear thermal expansion coefficients between the fused silica substrate (0.5×10^{-6} ˚C^{-1}) and the $BiVO_4$ (15.3×10^{-6} ˚C^{-1}) [35], which generates stress during the cooling, leading to a stress relaxation mechanism by cracking. The Bi, V, and O elemental distribution maps showed that all the elements were distributed uniformly throughout the film. This reveals the favorable and uniform formation of $BiVO_4$ on the surface. The quantitative chemical analysis obtained by EDS confirmed that the atomic ratio of Bi:V was 1:1.

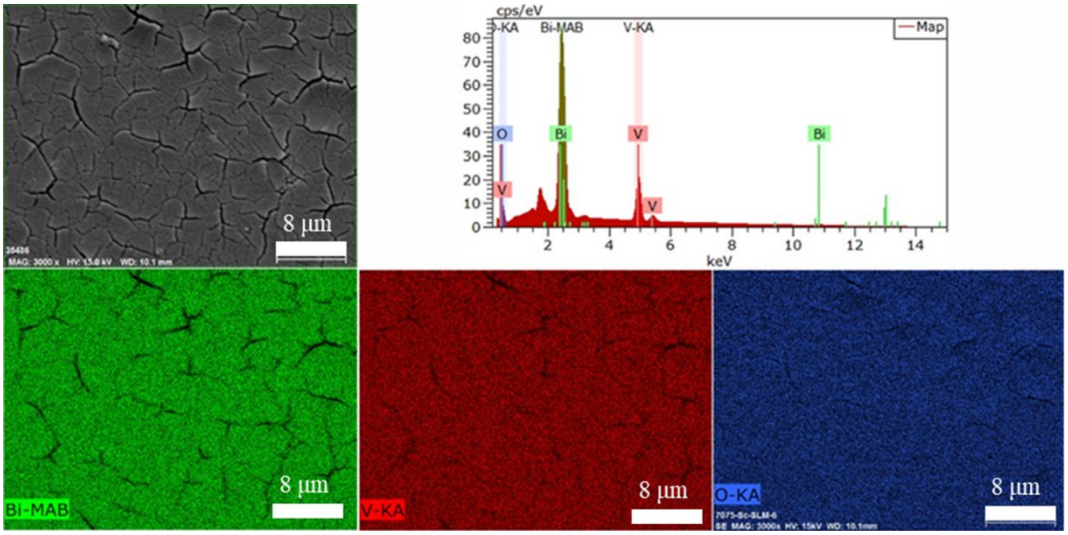

Fig. 3. FESEM image with the EDS spectrum and elemental distribution maps corresponding to a $BiVO_4$ thin film after annealing for 2 h at 450 ˚C in the air.

3.2. Sputtering pressure effect

Fig. 4 (a), (b), (c), and (d) show the FESEM observations of top surface morphology and brittle fracture cross-section of the films deposited on fused silica at different total pressures (2.5, 4.5 and 9.5 Pa) after annealing at 450 ˚C for 2 h under air, except for the sample shown in Fig. 4 (a) which was as-deposited at a total pressure of 4.5 Pa. The thickness of the samples for this part is kept in a close range (700 - 800 nm). Fig. 4 (a) exhibits that the as-deposited

film is dense without apparent cracks and black points which are observable on the annealed samples. As for the annealed samples, it is clear that the film morphology changes as a function of total pressure. The top surface of the coating deposited at 2.5 Pa looks glassy, and for the thin film deposited at 4.5 Pa, it is rather granular, while at 9.5 Pa, the morphology seems finer. The cross-section observations of the films deposited at 2.5 Pa exhibit a fairly dense morphology with a high relative amount of cracks compared to the films deposited at higher total pressure which develop a rather columnar morphology at 4.5 Pa, or which surprisingly becomes dense again at 9.5 Pa. It has been mentioned that total pressure can strongly affect the mechanism of film growth [25]. However, the morphology change after annealing does not correspond to the expected modification with the total sputtering pressure increase. According to the well-known structural zone model, the development of a columnar morphology leading to a rough surface is expecting at low deposition temperature and high total sputtering pressure, which is our case. Furthermore, it is noteworthy that all deposited film after annealing shows the presence of nanometric black points (< 100 nm) in secondary electrons micrographs showing the presence of nanopores deep enough so that no electrons can escape (> ~ 20 nm). The atomic composition being constant during the annealing, preferential evaporation of cations cannot explain the formation of the nanopores. The formation of similar nanopores was observed in the films having low melting elements [26, 27, 30] after their ionic irradiation in reason of local temperature elevation, and also in bonding formed from solid-liquid interdiffusion [39–41]. The annealing temperature largely exceeding the Bi melting point (271 ˚C), Bi melts allowing a fast diffusion of V and O atoms into the molten Bi, leading to the solidification of $BiVO_4$ [42], and to the vacancies coalescence to form nanopores [43] along with tensile stress which adds to the thermal stress. This could imply that Bi is not fully oxidized during the sputtering process, subsequently, the small submicron regions in the film structure remain in the metallic state which abide by their metallic properties, including having

a relatively low melting point. This allows them to melt during post-annealing treatment. As a result, this phenomenon could be responsible for the difference in morphology predicted by the structural zone model.

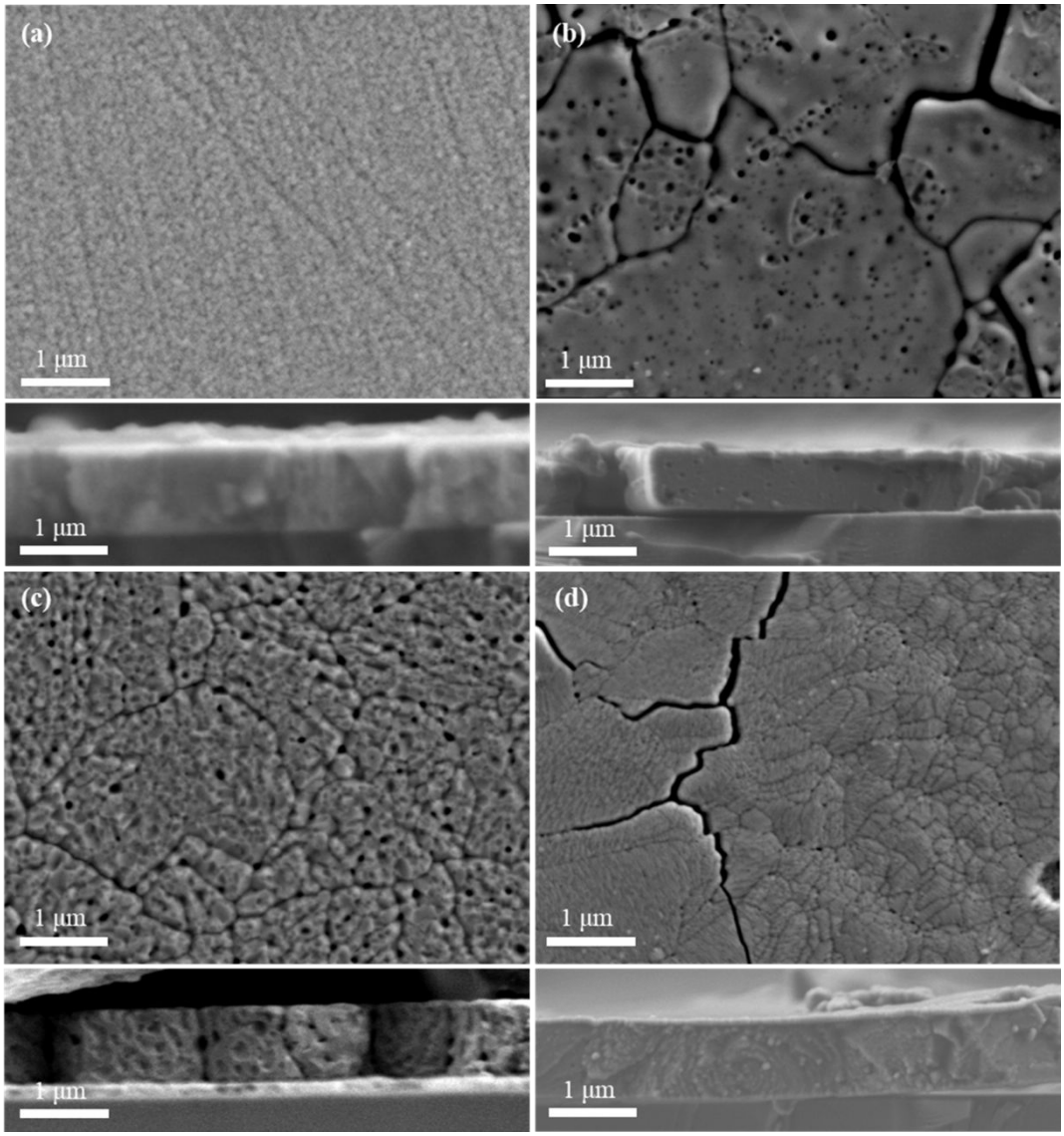

Fig. 4. FESEM images of the top surface and brittle-fracture cross-section of the thin films deposited on fused silica substrate at different total pressures of (a) As-deposited at 4.5 Pa and annealed films at 450 ˚C in air deposited at (b) 2.5, (c) 4.5, and (d) 9.5 Pa.

To assess the effect of the morphology on the film properties, caused by the change in sputtering pressure, the UV-Vis spectrophotometric technique is employed to obtain the transmission/reflectance spectra, and to determine the absorption coefficient, band gap,

refractive index, and porosity values. Fig. 5 shows the optical properties of the samples deposited at 2.5, 4.5, and 9.5 Pa, and annealed at 450 ˚C after 2 h in air. Fig 5. (a) shows the transmission spectra of the samples as a function of wavelength. The oscillations in the spectra in the NIR (Near-Infrared) and visible range are due to the interference of incident light after passing through different mediums (superstrate, film, and substrate), and it mainly depends on the refractive index and thickness of the thin films. The sudden fall in the transmission spectra in the visible region near 500 nm is the result of electronic interband absorption. The inset graph exhibits the reflectance spectra that underwent the same oscillations due to the interference of light as well. The comparison of the transmittance and reflectance spectra before and after annealing shows that not only the crystallization of the films decreases the transparency of the film but also the amplitude of fringes, which is primarily related to the refractive index of the film. The reduction of the transparency after annealing and the behavior of the transmission and reflectance close to the absorption edge could be ascribed to the formation of porosity, and hence to the scattering of light in the film by the nanopores and the related roughness. Fig. 5 (b) shows the absorption spectra of the films as a function of wavelength in the UV-Vis range, which were calculated using the following equation [20]:

$$\alpha(\lambda) = \frac{1}{t} \ln\left(\frac{1 - R(\lambda)}{T(\lambda)}\right) \quad (2)$$

Where t is the film thickness, $\alpha(\lambda)$, $R(\lambda)$, $T(\lambda)$ are the absorption, reflectance, and transmission values, respectively as a function of wavelength. The absorption edges for the samples deposited at 2.5, 4.5, and 9.5 Pa are 470, 508, and 490 nm, respectively. Thus, the sample deposited at 4.5 Pa absorbs more visible-light photons, consequently harvesting solar energy more effectively. The inset graph depicts the Tauc plot of the samples, which is employed to calculate the bandgap values through the following equation [20]:

$$(\alpha h\nu)^{1/n} = A(h\nu - E_g) \quad (3)$$

Here, hν is the energy of the photons (*h* is the Planck constant and *v* is the photon's frequency), *A* is a constant, and E_g is the bandgap energy of the material. Based on the literature, $BiVO_4$ is assumed to be a direct bandgap [44], thus the n is set to 0.5. The sample deposited at 4.5 Pa enjoys the lowest bandgap (2.44 eV) comparing to those deposited at higher or lower total pressures (2.64 and 2.53 eV, respectively). Fig. 5 (c) shows the pore size distribution for films deposited in different sputtering pressures. It can be seen that the average pore size for each sample is in the 20-40 nm range. Fig. 5 (d) displays the correlation of the porosity and the refractive index with the sputtering pressure. For calculating the porosity two technique is utilized. The image processing program method (IPM) is used to calculate the porosity and pore size distribution based on the SEM top surface micrographs. A downside to this technique is the incapability to take the depth of pores or closed pores into account. The spectrophotometric method (SM) was also used to calculate the porosity, thickness, and refractive index of the thin films. It relies on the interference in the experimental transmission/reflectance spectra to fit with an optical model of the refractive index which in this case is a two-term Cauchy's equation valuable for low absorption range ($\lambda > 1000$ nm in our case), assuming that the light absorption is insignificant and the light diffusion has a negligible effect in this wavelength range (1000-2600 nm) [45]:

$$n(\lambda) = C_1 + \frac{C_2}{\lambda^2} \quad (4)$$

Where n is the refractive index as a function of wavelength, λ is the wavelength of the incident light, and C_1 and C_2 are constants. The refractive index far from the absorption edge is then about 2.4 except for the annealed film deposited at 4.5 Pa (1.85). This value is in agreement with the refractive index range determined from density functional theory calculations (2.5 – 2.7) [35].

To calculate the film porosity, the volume averaging theory model is employed which is described via the following equation [45]:

$$n^2_{eff,\lambda c} = \Phi n^2_{dc} + (1 - \Phi) n^2_c \quad (5)$$

In this equation, the film is assumed as a composite of a continuous phase and a dispersed phase (air). The n_{eff}, n_c, and n_d are the refractive indexes of the composite, reference $BiVO_4$, and air respectively and Φ is the film porosity. Although this measurement is only semi-quantitative, the determination of the porosity from the optical properties is certainly more accurate taking the wider range of nanosize pores into account, unlike the IPM. The spectrophotometric results concerning the porosity are in agreement with the SEM observations in Fig. 4, which shows the highest value of porosity for the sample deposited at 4.5 Pa (52 % SM, 36% IPM) comparing to the other two, which are less than 10 %. It is well accepted that the sputtering pressure affects the deposition rate in agreement with the previous report [46]. Here, the mean deposition rate for the processes at 2.5, 4.5 and 9.5 Pa are around 6, 4 and 2.5 nm/s. On the other hand, the sputtering pressure and subsequently the deposition rate could have an impact on the crystallinity [46] and growth mechanism [25]. Therefore, various deposition rates might lead to a variety of distributions and quantities of the aforementioned submicron metallic regions, resulting in different values of porosity.

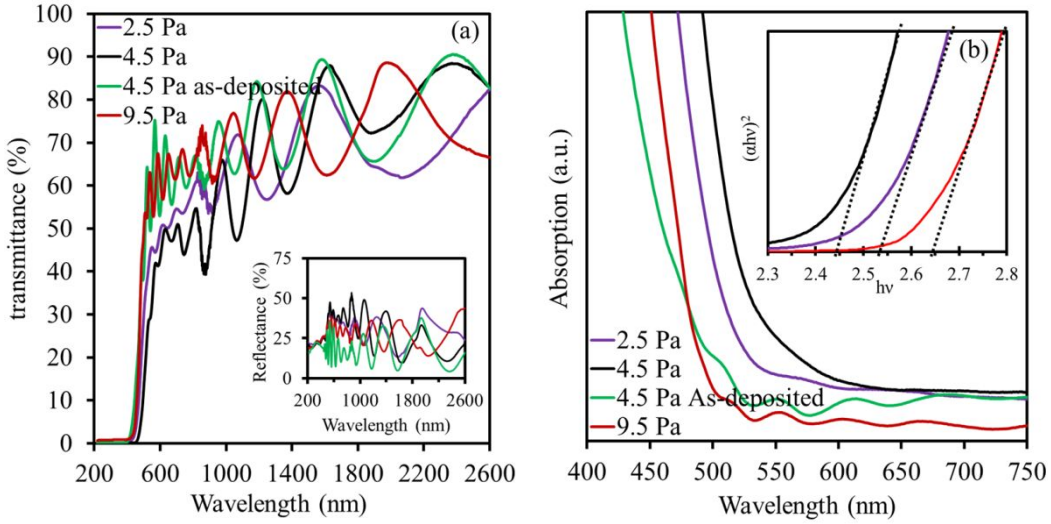

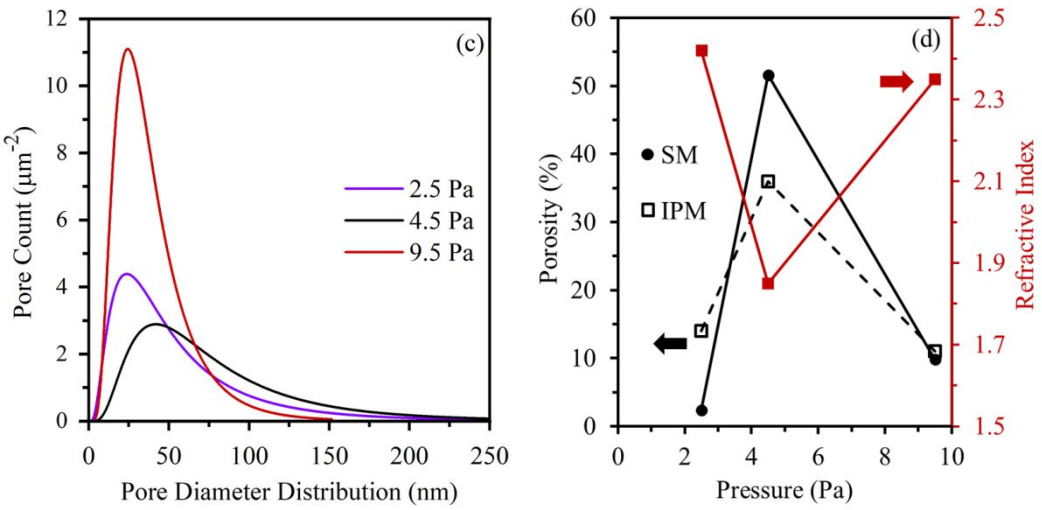

Fig. 5 (a) The transmittance spectra of the samples deposited at different total pressures. The inset graph shows their reflectance spectra, (b) the absorption spectra of the samples and the inset graph shows the bandgap using Tauc plot, (c) the pore size distribution, and (d) shows the porosity (left axis) and the refractive index in 1000-2600 nm range (right axis) as a function of sputtering pressure.

Fig. 6 (a) shows the photodegradation rate of RhB in a visible-light-driven photocatalytic experiment at pH = 3 for the samples deposited at 2.5, 4.5, and 9.5 Pa on fused silica substrate after 2 h of annealing at 450 ˚C in air. The inset graph exhibits the linear regression of ln C_0/C against time, in which rate constants of the photoreactions are extracted from its slope. Fig 6 (b) depicts the k′ values corresponding to each photocatalyst as a function of total pressure. The thin film deposited at 4.5 Pa managed to photodegrade 26 % (k′ = 0.041 h^{-1}) of the concentration of the solution in 7 h, while this value for the thin films deposited in higher or lower total pressure was less than 7 % (k′ = 0.0123, 0.005 h^{-1}, respectively). Separate experiments were conducted to ensure that the results are exclusively related to the photocatalytic degradation process. No activity has been observed without the catalysts under illumination (the blank test). The results obtained from Fig. 6 and Fig. 5 share some key features. The most photoactive sample (deposited at 4.5 Pa with 26 % degradation after 7 h) also enjoys the lowest bandgap combined with the highest percentage of nanosize porosity. In

catalytic reactions, the porous materials are advantageous and preferred, since, on one hand, porosity provides a larger surface for the reaction to occur, provided the solution can wet the open pores to benefit the large surface area. On the other hand, in thin films, the porosity affects light absorption through light scattering in the film, making the absorption of photons more effective. It may be worth mentioning that the crystallite size for the samples deposited in 2.5, 4.5, and 9.5 Pa are 47, 47, 59 nm respectively, concluding that the photocatalytic performance is not necessarily controlled by the microstructure.

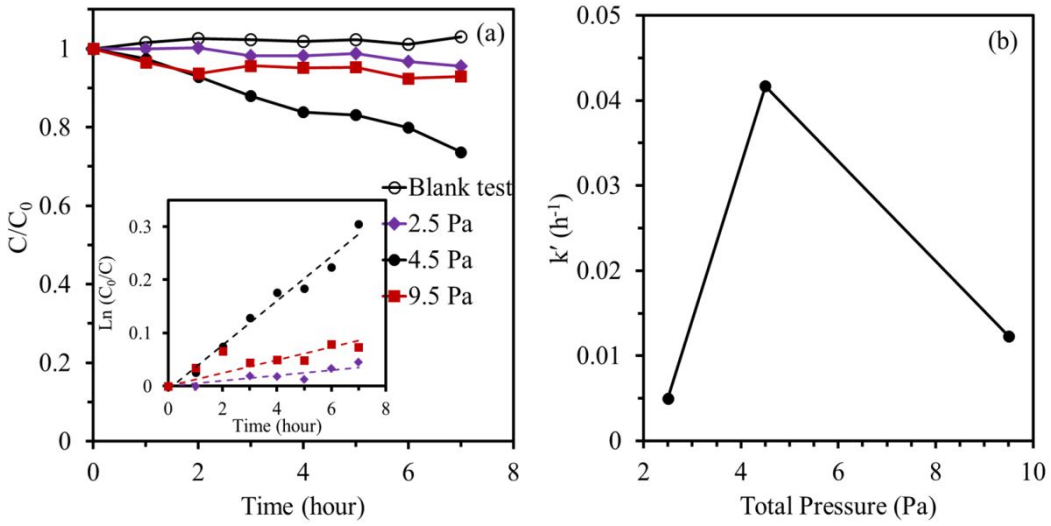

Fig. 6 (a) The RhB degradation rate under visible light irradiation in the presence of the photocatalysts deposited at 2.5, 4.5, and 9.5 Pa. The inset graph shows the linear regression of the Ln (C_0/C) versus time. (b) The k′ values of the photodegradation of the thin films against total pressure.

3.3. Substrate effect

Fig. 7 provides information about the thin films deposited on different substrates (alumina, silicon, and fused silica) at a total pressure of 4.5 Pa after 2 h of annealing at 450 ˚C in the air with a thickness of 705 ± 10 nm, and their respective photodegradation rate of the RhB solution under visible light irradiation at pH = 3. The thin film deposited on silicon managed to

photodegrade the solution by 53 % in 7 h, which was more than 4 times the photodegradation

by the film deposited on alumina (12 %), and this amount was almost two-fold comparing to the photodegradation achieved the film deposited on fused silica (26%). The inset graph shows the linear regression of the ln (C_0/C) versus time, whose slope gives the rate constant. It clearly shows the superiority of the film deposited on silicon ($k' = 0.099\ h^{-1}$) comparing to the other substrates ($k' = 0.019$ and $0.042\ h^{-1}$ for alumina and fused silica substrates, respectively). It is interesting to compare these results with those in the literature. Zhang et. al. [47] synthesized Y-doped $BiVO_4$ thin films by a polymeric method and evaluated the photodegradation of RhB solution (100 mL, 0.2 mg/L) under visible light (Xe-300 W, $\lambda > 420$ nm). They observed 18 % of photodegradation after 3 h of illumination in their optimal condition. Zhou et. al. [48] produced $BiVO_4$ thin films for photoelectrochemical purposes by dip-coating technique and observed 10 % degradation of bis-Phenol (75 mL, 10 mg/L) under 5 h of visible-light illumination (Xe-150 W) as their best photocatalytic performance. Silver-doped $BiVO_4$ powders have also been synthesized by chemical routes for photodegradation of RhB and Methyl Orange (100 ml, 10 mg/L) and achieved 31 % (3 h, Xe-300 W) [49] and 24 % (4 h, Xe-500 W) [50] photodegradation, respectively concerning their pristine $BiVO_4$ samples. This proves that producing $BiVO_4$ thin-film photocatalysts via reactive magnetron sputtering is interesting considering the aforementioned advantages including stable low-cost high throughput industrial productions. The XRD patterns for each sample are presented in Fig. 7 (b), which exhibit the crystal structure of the films. Since the silicon substrate has a very intense peak at 33.41˚ corresponding to (111) crystallographic plane, the XRD patterns are presented in the 2θ range of 35 to 60˚. The XRD patterns are similar for all of the substrates. The average crystallite size of $BiVO_4$ deposited on alumina, silicon, and fused silica are 52, 56, and 47 nm, respectively. There is no pronounced change in the preferential orientation of the film. The monoclinic $BiVO_4$ phase is successfully formed on the alumina, silicon, and fused silica substrates after 2 h of annealing at 450 ˚C in the air with no observations of contamination,

unlike the glass substrate that was discussed earlier. Fig. 7 (c) shows the pore size distribution using IPM and the average value is in the 20-40 nm range. Fig. 7 (d) exhibits the porosity employing IPM. It can be seen that the film deposited on silicon enjoys a porosity as high as the film deposited on fused silica (36 %). Spectrophotometric technique results for the samples deposited on alumina and fused silica cannot be obtained due to the lack of transparency and inability to measure the transmission/reflectance spectra. The FESEM observations of the top surface and brittle fracture cross-sections of the alumina and silicon samples are provided in Fig. 7 (e), and in Fig. 4 (b) for the sample deposited on fused silica. The film deposited on silicon enjoys a very high porosity, unlike the film deposited on alumina which exhibits a more corrugated surface. The coefficients of thermal expansion of silicon, fused silica, and alumina substrates being 2.6×10^{-6} ˚C^{-1}, 0.5×10^{-6} ˚C^{-1} and 8.1×10^{-6} ˚C^{-1}, respectively, and relating to the $BiVO_4$ (see section 3.2 sputtering pressure effect) show that the film develops tensile stress and cracks in the cooling mainly for silicon or fused silica substrates, but do not explain the efficiency of the silicon substrate. The thermal conductivity of silicon is about 100 and 10 times greater than that of fused silica and alumina. This would lead to a faster thermal equilibrium for silicon substrate, and thus to a more efficient diffusional process. Moreover, the silicon has a reflective surface that makes the incident photons pass through the films more than the other substrates raising the chance of photon absorption by the film. Based on the investigation in this part, the silicon is proved a superior substrate for $BiVO_4$ thin films in photocatalytic activity. Therefore, the sample deposited on silicon is chosen for the study of the effect of pH on photocatalytic degradation.

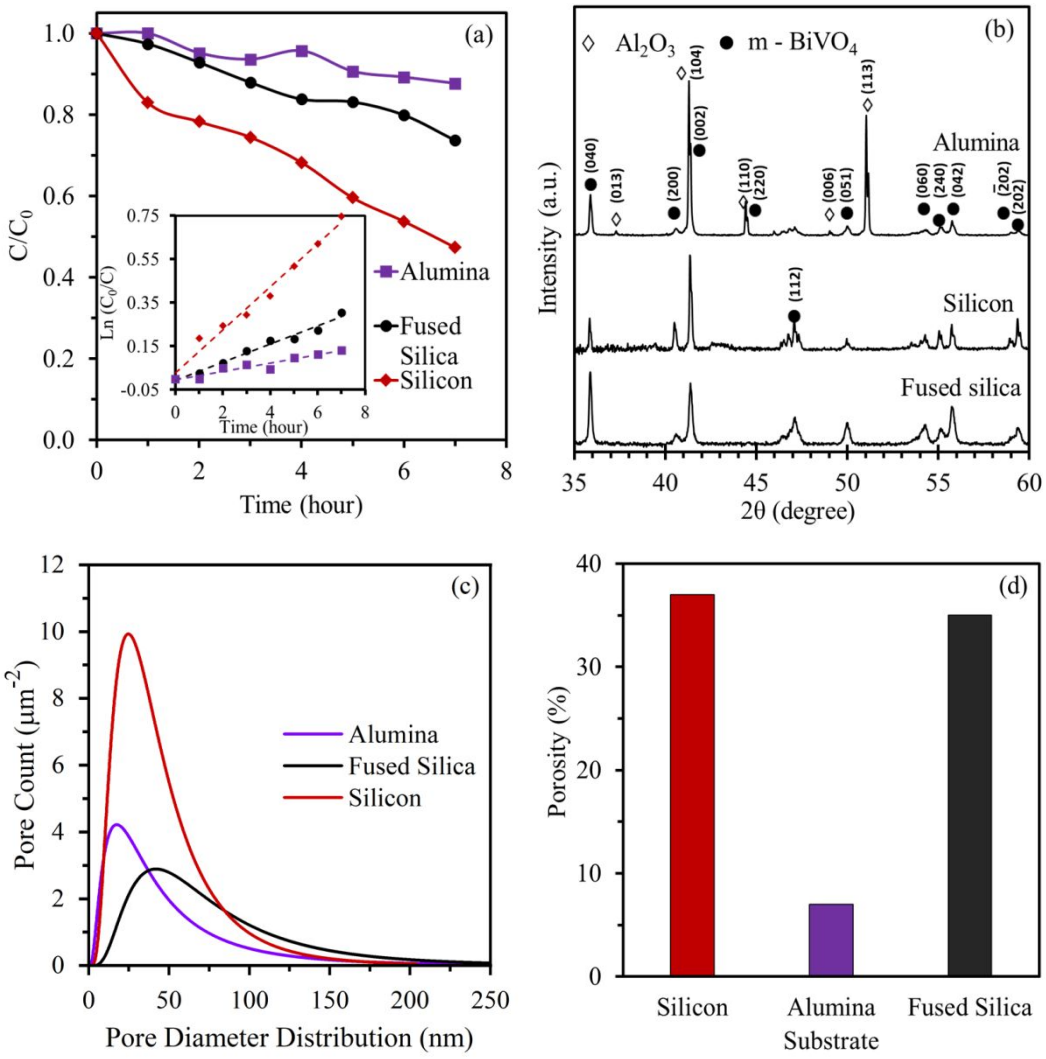
(a)
C/C0
Time (hour)
Ln (C0/C)
Alumina
Fused Silica
Silicon
(b)
◇ Al2O3
● m - BiVO4
Intensity (a.u.)
2θ (degree)
Alumina
Silicon
Fused silica
(c)
Pore Count (μm-2)
Pore Diameter Distribution (nm)
Alumina
Fused Silica
Silicon
(d)
Porosity (%)
Silicon
Alumina
Fused Silica
Substrate

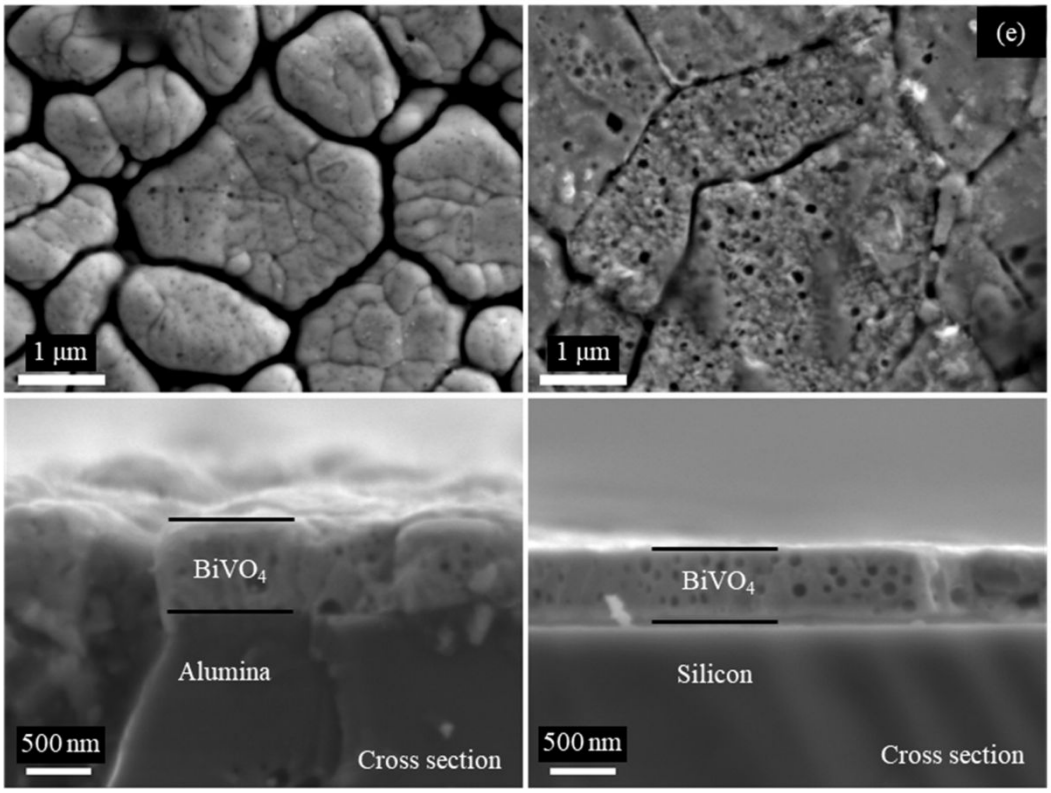

Fig. 7 (a) The RhB photodegradation rate under visible light irradiation for the photocatalysts with different substrates (alumina, fused silica, and silicon). The inset graph shows the linear regression of the ln (C_0/C) versus time. (b) The XRD patterns corresponding to the film with different substrates and (c) the pore size distribution, (d) the porosity values using the IPM method, and (e) FESEM observations of the top surface and brittle fracture cross-section for the thin films deposited on the alumina and silicon substrates.

3.4. Photodegradation mechanism of RhB

Fig. 8 (a) illustrates a schematic view of the photocatalytic degradation of RhB by $BiVO_4$ thin films under visible light illumination. Photodecomposition of RhB follows two main pathways: N-deethylation and chromophore cleavage [51]. During the N-deethylation process, a hypsochromic shift is always observed due to absorption characteristics of the byproducts whereas no shift is prompted by the chromophore cleavage [52, 53]. In

consideration of temporal UV-Vis absorption spectra shown in Fig. 8 (b), it can be verified that

the photodecomposition of RhB by the $BiVO_4$ thin-film photocatalysts at pH = 3, follows the chromophore cleavage pathway since no hypsochromic shift is observed in the spectra. The mechanism experiments in the literature using scavengers show a collective agreement that the photogenerated holes and hydroxyl radicals play the most important role in photodecomposition of organic pollutants by $BiVO_4$ photocatalysts thanks to a well-positioned valence band, whereas the $^{\bullet}O_2^-$ is much less effective due to the positive potential of the conduction band [54–56]. The formation of the oxidative species involved in $BiVO_4$ photoactivity are suggested in the literature via the reactions of 6 to 8 [57]:

$$h_{VB}^+ + H_2O \rightarrow H^+ + {}^{\bullet}OH + e^- \quad (6)$$

$$h_{VB}^+ + OH^- \rightarrow {}^{\bullet}OH + e^- \quad (7)$$

$$h_{VB}^+ + RhB \rightarrow \text{Oxidation products} \quad (8)$$

The estimation of conduction and valence band edge position is also calculated with the equation 9 and 10:

$$E_{CB} = \chi - E_0 - 0.5E_g \quad (9)$$

$$E_{VB} = E_{CB} + E_g \quad (10)$$

Here, E_{CB}, E_{VB}, χ, and E_0 are conduction band edge potential energy (0.31 V), valence band edge potential energy (2.75 V), the electronegativity of the bulk $BiVO_4$ (6.035), and the energy of a free electron in the hydrogen scale (-4.5 eV), respectively [57–59].

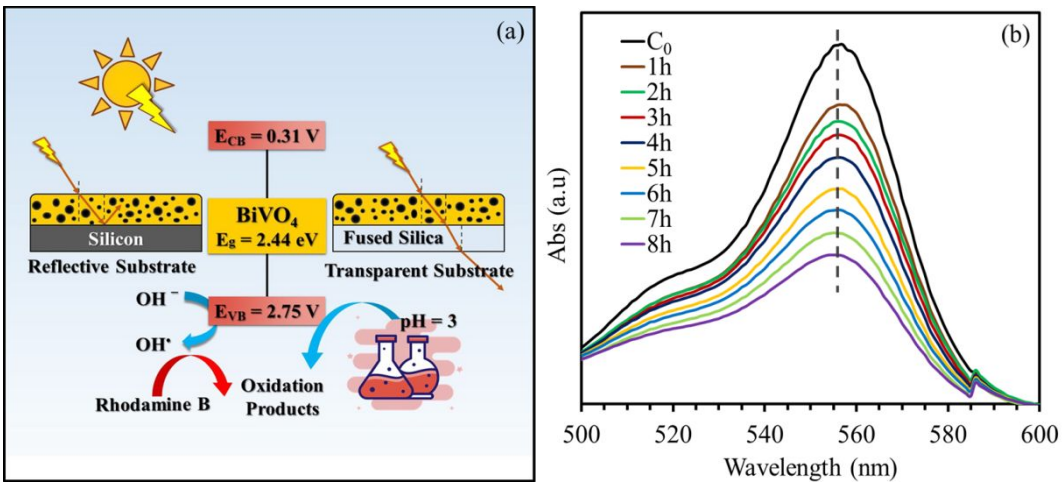

Fig. 8 (a) schematic of photocatalytic degradation of RhB solution by $BiVO_4$ thin films deposited on silicon and fused silica substrates at pH = 3 under visible light illumination. (b) temporal UV-Vis absorption spectra of RhB photodegradation at pH = 3 by $BiVO_4$ thin-film photocatalyst deposited on silicon

4. Conclusions

The following conclusions can be made from this work:

(1) Nanoporous $BiVO_4$ thin films were successfully synthesized via a novel route using the reactive DC magnetron sputtering deposition method, comparatively at various total pressures and on a variety of substrates, followed by a post-annealing treatment in the air at different temperatures to crystallize the photoactive monoclinic scheelite phase.

(2) The crystal structure started to form at 250˚C for the film deposited on fused silica, it was stable up to 600˚C. The film deposited on glass crystalized at 300˚C but soon started to disintegrate at 350˚C due to sodium contamination. The crystallite size increased by the rise of temperature.

(3) The films were deposited at 2.5, 4.5 and 9.5 Pa on fused silica and annealed at 450˚C to investigate the effect of total sputtering pressure on the film properties.

(4) FESEM observations, spectrophotometric results, and photocatalytic experiments exhibited that the film deposited at 4.5 Pa with nanoporous morphology had the highest porosity (52 %), fewer cracks, lowest bandgap value (2.44 eV), and highest photoactivity under visible light illumination (26 % of RhB photodegradation in 7 h).

(5) The nature of the substrate was also investigated as a deposition parameter. In addition to glass and fused silica, thin films were also deposited on silicon and alumina.

(6) XRD results showed the proper formation of the monoclinic scheelite structure of the films deposited on both silicon and alumina annealed at 450 ˚C with no contamination.

While FESEM results exhibited that the film deposited on silicon formed a higher amount of porosity, the morphology of the film deposited on alumina was rather corrugated than porous.

(7) The film deposited on silicon showed superiority in terms of photocatalytic performance (53 % after 7 h) probably owing to higher porosity and light absorption efficiency due to the reflective surface of the substrate.

(8) Lack of hypsochromic shifts verified the chromophore cleavage process as the dominant pathway of RhB photodegradation by $BiVO_4$ thin films deposited on silicon substrates at pH = 3.

Conflict of interest

The authors declare that they have no conflict of interest.

Acknowledgments

The authors would like to acknowledge the supports of this study by the Iran National Science Foundation (project No: 98001285) and Pays de Montbéliard Agglomération for the support of this work.

References

[1] HASHIMOTO K, IRIE H, FUJISHIMA A. TiO_2 photocatalysis: A historical overview and future prospects [J]. Japanese Journal of Applied Physics, Part 1: Regular Papers and Short Notes and Review Papers, 2005, 44: 8269–8285.

[2] BYRNE C, SUBRAMANIAN G, PILLAI SC. Recent advances in photocatalysis for environmental applications [J]. Journal of Environmental Chemical Engineering, 2018, 6: 3531–3555.

[3] ESMAILI H, KOTOBI A, SHEIBANI S, et al. Photocatalytic degradation of

methylene blue by nanostructured Fe/FeS powder under visible light [J]. International Journal of Minerals, Metallurgy and Materials, 2018, 25: 244–252.

[4] ABDOLHOSEINZADEH A, SHEIBANI S. Enhanced photocatalytic performance of Cu_2O nano-photocatalyst powder modified by ball milling and ZnO [J]. Advanced Powder Technology, 2020, 31: 40–50.

[5] AKHAVAN O, CHOOBTASHANI M, GHADERI E. Protein degradation and RNA efflux of viruses photocatalyzed by graphene-tungsten oxide composite under visible light irradiation [J]. Journal of Physical Chemistry C, 2012, 116: 9653–9659.

[6] AHADI S, MOALEJ NS, SHEIBANI S. Characteristics and photocatalytic behavior of Fe and Cu doped TiO_2 prepared by combined sol-gel and mechanical alloying [J]. Solid State Sciences, 2019, 96: 105975.

[7] MONTAKHAB E, RASHCHI F, SHEIBANI S. Modification and photocatalytic activity of open channel TiO_2 nanotubes array synthesized by anodization process [J]. Applied Surface Science, 2020, 534: 147581.

[8] NAKHATE GG, NIKAM VS, KANADE KG, et al. Hydrothermally derived nanosized Ni-doped TiO_2: A visible light driven photocatalyst for methylene blue degradation [J]. Materials Chemistry and Physics, 2010, 124: 976–981.

[9] SU X, LIU C, LIU Y, et al. Construction of $BiVO_4$ nanosheets@WO_3 arrays heterojunction photoanodes by versatile phase transformation strategy [J]. Transactions of Nonferrous Metals Society of China, 2021, 31: 533–544.

[10] WANG M, YANG G Jun, YOU M Yan, et al. Effects of Ni doping contents on photocatalytic activity of B-$BiVO_4$ synthesized through sol-gel and impregnation two-step method [J]. Transactions of Nonferrous Metals Society of China (English Edition), 2017, 27: 2022–2030.

[11] LIU L, HU T, DAI K, et al. A novel step-scheme $BiVO_4$/Ag_3VO_4 photocatalyst for

enhanced photocatalytic degradation activity under visible light irradiation [J]. Chinese Journal of Catalysis, 2020, 42: 46–55.

[12] TOKUNAGA S, KATO H, KUDO A. Selective Preparation of Monoclinic and Tetragonal $BiVO_4$ with Scheelite Structure and Their Photocatalytic Properties [J]. Chemistry of Materials, 2001, 13: 4624–4628.

[13] DOLIĆ SD, JOVANOVIĆ DJ, SMITS K, et al. A comparative study of photocatalytically active nanocrystalline tetragonal zircon-type and monoclinic scheelite-type bismuth vanadate [J]. Ceramics International, 2018, 44: 17953–17961.

[14] MENG X, ZHANG Z. Bismuth-based photocatalytic semiconductors: Introduction, challenges and possible approaches [J]. Journal of Molecular Catalysis A: Chemical, 2016, 423: 533–549.

[15] HU Y, FAN J, PU C, et al. Facile synthesis of double cone-shaped $Ag_4V_2O_7/BiVO_4$ nanocomposites with enhanced visible light photocatalytic activity for environmental purification [J]. Journal of Photochemistry and Photobiology A: Chemistry, 2017, 337: 172–183.

[16] WANG M, NIU C, LIU J, et al. Effective visible light-active nitrogen and samarium co-doped $BiVO_4$ for the degradation of organic pollutants [J]. Journal of Alloys and Compounds, 2015, 648: 1109–1115.

[17] LI H Bin, ZHANG J, HUANG G You, et al. Hydrothermal synthesis and enhanced photocatalytic activity of hierarchical flower-like Fe-doped $BiVO_4$ [J]. Transactions of Nonferrous Metals Society of China (English Edition), 2017, 27: 868–875.

[18] RUAN PC, CHEN HF, HU JL, et al. Preparation and Activities of Visible-Light-Driven $BiVO_4$ by Doping Ag via Solid State Method [J]. Key Engineering Materials, 2016, 703: 326–330.

[19] MERUPO Vi, VELUMANI S, OZA G, et al. High Energy Ball-Milling Synthesis of

Nanostructured Ag-Doped and $BiVO_4$-Based Photocatalysts [J]. ChemistrySelect, 2016, 1: 1278–1286.

[20] SARKAR S, DAS NS, CHATTOPADHYAY KK. Optical constants, dispersion energy parameters and dielectric properties of ultra-smooth nanocrystalline $BiVO_4$ thin films prepared by rf-magnetron sputtering [J]. Solid State Sciences, 2014, 33: 58–66.

[21] ZEMAN P, TAKABAYASHI S. Nano-scaled photocatalytic TiO_2 thin films prepared by magnetron sputtering. In: *Thin Solid Films*. Elsevier, 2003, pp. 57–62.

[22] GUILLÉN C, HERRERO J. TiO_2 coatings obtained by reactive sputtering at room temperature: Physical properties as a function of the sputtering pressure and film thickness [J]. Thin Solid Films, 2017, 636: 193–199.

[23] MALATHI A, MADHAVAN J, ASHOKKUMAR M, et al. A review on $BiVO_4$ photocatalyst: Activity enhancement methods for solar photocatalytic applications. Elsevier B.V.

[24] SAMSUDIN MFR, SUFIAN S, HAMEED BH. Epigrammatic progress and perspective on the photocatalytic properties of $BiVO_4$-based photocatalyst in photocatalytic water treatment technology: A review [J]. Journal of Molecular Liquids, 2018, 268: 438–459.

[25] ANDERS A. A structure zone diagram including plasma-based deposition and ion etching [J]. Thin Solid Films, 2010, 518: 4087–4090.

[26] YANAGIDA Y, OISHI T, MIYAJI T, et al. Nanoporous structure formation in Gasb, Insb, and Ge by Ion beam irradiation under controlled point defect creation conditions [J]. Nanomaterials, 7. Epub ahead of print 11 July 2017. DOI: 10.3390/nano7070180.

[27] NITTA N, HASEGAWA T, YASUDA H, et al. Void Formation and Structure Change Induced by Heavy Ion Irradiation in GaSb and InSb. [J]. MATERIALS TRANSACTIONS, 2010, 51: 1059–1063.

[28] WILSON IH. The effects of self-ion bombardment (30-500 keV) on the surface topography of single-crystal germanium [J]. Journal of Applied Physics, 1982, 53: 1698–1705.

[29] ALKHALDI HS, KREMER F, BIERSCHENK T, et al. Porosity as a function of stoichiometry and implantation temperature in Ge/$Si_{1-x}Ge_x$ alloys [J]. Journal of Applied Physics, 119. Epub ahead of print 2016. DOI: 10.1063/1.4942995.

[30] MIYAJI T, NITTA N. Nanoporous Structure Formation on the Surface of InSb by Ion Beam Irradiation [J]. Nanomaterials, 2017, 7: 204.

[31] YAZDI M A P, BRIOIS P, BILLARD A. Influence of the annealing conditions on the structure of $BaCe_{1-x}Y_xO_{3-\alpha}$ coatings elaborated by DC magnetron sputtering at room temperature [J]. Materials Chemistry and Physics, 2009, 117: 178–182.

[32] BAKHTIARNIA S, SHEIBANI S, BILLARD A, et al. Enhanced photocatalytic activity of sputter-deposited nanoporous $BiVO_4$ thin films by controlling film thickness [J]. Journal of Alloys and Compounds, 2021, 879: 160463.

[33] KUMAR KV, PORKODI K, ROCHA F. Langmuir-Hinshelwood kinetics - A theoretical study [J]. Catalysis Communications, 2008, 9: 82–84.

[34] HOFFMAN D W, THORNTON J A. The compressive stress transition in Al, V, Zr, Nb and W metal films sputtered at low working pressures [J]. Thin Solid Films, 1977, 45: 387–396.

[35] SINCLAIR DC, WATSON CJ, ALAN HOWIE R, et al. $NaBi_3V_2O_{10}$: A new oxide ion conductor [J]. Journal of Materials Chemistry, 1998, 8: 281–282.

[36] AUBRY E, LAMBERT J, DEMANGE V, et al. Effect of Na diffusion from glass substrate on the microstructural and photocatalytic properties of post-annealed TiO_2 films synthesized by reactive sputtering [J]. Surface and Coatings Technology, 2012, 206: 4999–5005.

[37] VENKATESAN R, VELUMANI S, ORDON K, et al. Nanostructured bismuth vanadate ($BiVO_4$) thin films for efficient visible light photocatalysis [J]. Materials Chemistry and Physics, 2018, 205: 325–333.

[38] CULLITY BD. Elements of X-RAY Diffraction [M]. Second edition. Reading Mass: Addison-Wesley Pub. Co., 1978.

[39] AASMUNDTVEIT K E, LU U T, WANG K, et al. Void formation in Cu-Sn Solid-Liquid Interdiffusion (SLID) bonding [C]// *2015 European Microelectronics Packaging Conference (EMPC)*. 2015, pp. 1–6.

[40] AASMUNDTVEIT KE, TEKSETH KR, BREIBY DW, et al. High-energy x-ray tomography for 3d void characterization in au-sn solid-liquid interdiffusion (SLID) bonds [C]// *2019 22nd European Microelectronics and Packaging Conference and Exhibition, EMPC 2019*. Institute of Electrical and Electronics Engineers Inc., 2019. Epub ahead of print 16 September 2019. DOI: 10.23919/EMPC44848.2019.8951843.

[41] DEILLON L, HESSLER-WYSER A, HESSLER T, et al. Solid-liquid interdiffusion (SLID) bonding in the Au-In system: Experimental study and 1D modelling. [J]. Journal of Micromechanics and Microengineering, 2015, 25: 125016.

[42] COOK G O, SORENSEN C D. Overview of transient liquid phase and partial transient liquid phase bonding. *Journal of Materials Science* 2011, 46: 5305–5323.

[43] KIM D, CHANG J, PARK J, et al. Formation and behavior of Kirkendall voids within intermetallic layers of solder joints [J]. Journal of Materials Science: Materials in Electronics, 22: 703–716.

[44] WALSH A, YAN Y, HUDA MN, et al. Band edge electronic structure of $BiVO_4$: Elucidating the role of the Bi s and V d orbitals. [J]. Chemistry of Materials, 2009, 21: 547–551.

[45] GALY T, MARSZEWSKI M, KING S, et al. Comparing methods for measuring

thickness, refractive index, and porosity of mesoporous thin films [J]. Microporous and Mesoporous Materials, 2020, 291: 109677.

[46] KIM D Y, KWON J H, JANG G S, et al. Effect of Pressure on the Film Deposition during RF Magnetron Sputtering Considering Charged Nanoparticles [J]. Coatings, 2021, 11: 132.

[47] ZHANG Y, YI Z, WU G, et al. Novel Y doped $BiVO_4$ thin film electrodes for enhanced photoelectric and photocatalytic performance [J]. Journal of Photochemistry and Photobiology A: Chemistry, 2016, 327: 25–32.

[48] ZHOU B, QU J, ZHAO X, et al. Fabrication and photoelectrocatalytic properties of nanocrystalline monoclinic $BiVO_4$ thin-film electrode [J]. Journal of Environmental Sciences, 2011, 23: 151–159.

[49] XU L, WEI Y, GUO W, et al. One-pot solvothermal preparation and enhanced photocatalytic activity of metallic silver and graphene co-doped $BiVO_4$ ternary systems [J]. Applied Surface Science, 2015, 332: 682–693.

[50] ZHANG A, ZHANG J. Synthesis and characterization of $Ag/BiVO_4$ composite photocatalyst [J]. Applied Surface Science, 2010, 256: 3224–3227.

[51] HE Z, SUN C, YANG S, et al. Photocatalytic degradation of rhodamine B by Bi_2WO_6 with electron accepting agent under microwave irradiation: Mechanism and pathway. [J]. Journal of Hazardous Materials, 2009, 162: 1477–1486.

[52] WANG Y, LU N, LUO M, et al. Enhancement mechanism of fiddlehead-shaped TiO_2 -$BiVO_4$ type II heterojunction in SPEC towards RhB degradation and detoxification [J]. Applied Surface Science, 2019, 463: 234–243.

[53] WANG P, CHENG M, ZHANG Z. On different photodecomposition behaviors of rhodamine B on laponite and montmorillonite clay under visible light irradiation [J]. Journal of Saudi Chemical Society, Epub ahead of print 2014. DOI:

10.1016/j.jscs.2013.11.006.

[54] LOPES O F, CARVALHO K T G, NOGUEIRA A E, et al. Controlled synthesis of $BiVO_4$ photocatalysts: Evidence of the role of heterojunctions in their catalytic performance driven by visible-light [J]. Applied Catalysis B: Environmental, 2016, 188: 87–97.

[55] XIE Q, HE W, LIU S, et al. Bifunctional S-scheme g-C_3N_4/Bi/$BiVO_4$ hybrid photocatalysts toward artificial carbon cycling [J]. Chinese Journal of Catalysis, 2020, 41: 140–153.

[56] SALEEM A, AHMED T, AMMAR M, et al. Direct growth of m-$BiVO_4$@carbon fibers for highly efficient and recyclable photocatalytic and antibacterial applications [J]. Journal of Photochemistry and Photobiology B: Biology, 2020, 213: 112070.

[57] FAKHRAVAR S, FARHADIAN M, TANGESTANINEJAD S. Excellent performance of a novel dual Z-scheme Cu_2S/Ag_2S/$BiVO_4$ heterostructure in metronidazole degradation in batch and continuous systems: Immobilization of catalytic particles on α-Al_2O_3 fiber [J]. Applied Surface Science, 2020, 505: 144599.

[58] NETHERCOT AH. Prediction of Fermi energies and photoelectric thresholds based on electronegativity concepts [J]. Physical Review Letters, 1974, 33: 1088–1091.

[59] BUTLER MA, GINLEY DS. Prediction of Flatband Potentials at Semiconductor-Electrolyte Interfaces from Atomic Electronegativities. [J]. Journal of The Electrochemical Society, 1978, 125: 228–232.